Acta Materialia 238 (2022) 118224

Contents lists available at ScienceDirect

Acta Materialia

journal homepage: www.elsevier.com/locate/actamat

Full length article

Improving the intermediate- and high-temperature strength of $L1_2$-$Co_3(Al,W)$ by Ni and Ta additions

Zhenghao Chen[a,b,*], Kyosuke Kishida[a,b], Haruyuki Inui[a,b], Martin Heilmaier[c], Uwe Glatzel[d], Gunther Eggeler[e]

[a] *Department of Materials Science and Engineering, Kyoto University, Kyoto 606-8501, Japan*
[b] *Center for Elements Strategy Initiative for Structure Materials (ESISM), Kyoto University, Sakyo-ku, Kyoto 606-8501, Japan*
[c] *Institute for Applied Materials (IAM-WK), Karlsruhe Institute of Technology (KIT), Engelbert-Arnold-Strasse 4, Karlsruhe 76131, Germany*
[d] *Metals and Alloys, University of Bayreuth, Prof.-Rüdiger-Bormann-Strasse. 1, Bayreuth 95447, Germany*
[e] *Lehrstuhl Werkstoffwissenschaft (WW), Institut für Werkstoffe, Ruhr-Universität Bochum, Universitätsstrasse 150, D, Bochum 44780, Germany*

ARTICLE INFO

Article history:
Received 20 June 2022
Revised 28 July 2022
Accepted 29 July 2022
Available online 30 July 2022

Keywords:
$L1_2$ compound
Co-based superalloys
High-temperature deformation
Dislocation structures, Transmission electron microscopy

ABSTRACT

The effects of Ni and Ta additions on the mechanical properties in the $L1_2$ compound $Co_3(Al,W)$, the strengthening phase of Co-based superalloys, have been investigated by compression tests between room temperature and 1000 °C, in order to elucidate the effects of stability of the $L1_2$ phase on the mechanical properties. The additions of Ni and Ta, both of which are $L1_2$-stabilizers that increase the $L1_2$ solvus temperature, increase the yield strength at intermediate and high temperatures. The strength increase is shown to be more significant as the amount of additions of these elements and thereby the stability of the $L1_2$ phase increases. Two factors account for the strength increase at intermediate temperatures: The reduction of the onset temperature of yield stress anomaly (YSA-onset) due to the increased complex stacking fault (CSF) energy and the increase in both the base strength and the intensity of the yield stress anomaly associated with an increased anti-phase boundary (APB) energy on (111) planes. The strength increase at high temperatures, on the other hand, arises from the increase in the peak temperature due to the increased $L1_2$ solvus temperatures. The increased strength of the $L1_2$ phase due to a higher phase stability thus partly accounts for the improved creep strength of Co-based superalloys upon alloying with Ni and Ta.

1. Introduction

Microstructures of the ternary Co-Al-W system consist of two phases, an ordered $Co_3(Al,W)$ phase ($L1_2$ crystal structure, usually designated as the γ' phase) and a face centered (fcc) Co-rich solid solution [1]. There has been a significant research activity in the development of Co-based superalloys where $Co_3(Al,W)$ is the strengthening phase [2–14]. There was initially an expectation that high-temperature mechanical properties of Co-based superalloys would outperform those of Ni-based superalloys. This was related to the fact that precipitation of the γ' phase in the γ matrix occurs coherently and forms cuboidal precipitates like in Ni-based superalloys with the advantage that both the melting temperature and the elastic stiffness are higher for Co than for Ni [15,16]. In spite of this early expectation, however, the high-temperature creep strength of Co-based superalloys which were so far developed are modest, only comparable to those for Ni-based superalloys of the first generation (such as IN100, NM002 and others) [2,4,11,14,17–23]. Many factors such as the low γ' solvus temperature [4,18], low γ' volume fractions at high temperatures [4], low high-temperature strength of the γ' phase [24,25] and positive lattice misfit between γ and γ' phases [26] were suggested as being responsible for this disappointing finding. It is important to note that the factors described above are all directly related to a lower phase stability of the γ' phase in these alloys [4,8,16,18,20]. Alloying elements that can increase the phase stability of the γ' phase (i.e. γ'-forming elements) have thus been investigated extensively, exploring whether one can benefit from the fact that elements like Ni, Ta and Ti are effective in increasing the γ' phase stability [27–33]. In fact, the creep properties of Co-based superalloys have been reported to improve considerably upon alloying with these elements to the level comparable to those of Ni-base superalloys of the second generation (such as RR2000, SRR 99 and others) [7,34]. This has been associated with an increased γ' solvus

---

[*] Corresponding author at: Department of Materials Science and Engineering, Kyoto University, Kyoto 606-8501, Japan.
E-mail address: chen.zhenghao.6e@kyoto-u.ac.jp (Z. Chen).

https://doi.org/10.1016/j.actamat.2022.118224

temperature as well as with an increased γ' volume fraction [7,34]. The strength of the γ' phase is also expected to be improved when these alloying elements are added, but nothing is known at present about whether or not and how a higher strength of the γ' phase contributes to an improved creep strength of Co-based alloys.

In the present study, we investigate the compression behavior of $L1_2$ compounds $Co_3(Al,W)$ with Ni and Ni+Ta additions in a temperature range from room temperature to 1000 °C. Emphasis is placed on the deformation microstructures of these $L1_2$ compounds through detailed transmission electron microscopy (TEM) investigations, paying special attention to how the anomalous increase in yield stress (often referred to as 'yield stress anomaly' in $L1_2$ compound research [35–41]) occurs in these $L1_2$ compounds, in comparison with the ternary $Co_3(Al,W)$ base alloy with a composition of Co-12 at.%Al-11 at.%W [25]. We will discuss how and why the mechanical properties of the $Co_3(Al,W)$ compounds change upon alloying with Ni and Ni+Ta and how the changes in mechanical properties of the γ' ($Co_3(Al,W)$) phase contribute to the improved high-temperature creep strength of Co-based superalloys.

2. Experiment procedures

Ingots with nominal compositions of $(Co_{0.9}Ni_{0.1})$-12 at.%Al-11 at.%W, $(Co_{0.8}Ni_{0.2})$-12 at.%Al-11 at.%W and $(Co_{0.8}Ni_{0.2})$-12 at.%Al-9 at.%W-2 at.%Ta were prepared by arc-melting using high-purity feed stock of the elements Co, Al, W, Ni and Ta under an Ar atmosphere. These alloys are referred to as 10Ni, 20Ni and 20Ni-2Ta alloys throughout this paper. These compositions were chosen for the following reasons. The high Ni-solubility allows to increase the γ' solvus temperature of γ/γ' two-phase Co-based alloys by sufficient amounts of Ni additions [11,25,30], even though small amounts of Ni are not very effective. On the other hand, the increase in the γ' solvus temperature of γ/γ' two-phase Co-based alloys by small additions of Ta or Ti addition is significant but the Ta and Ti solubilities are limited in general to a few at% [11,28,29,31]. Ingots were sealed in a quartz ampoule with Ar gas and annealed at 850 °C for 168 h followed by air cooling. All the three alloys exhibit columnar grains elongated in the thickness direction of the button ingots (i.e., in the heat-removal direction during solidification in arc-melting) with typical dimensions of 200~400 μm in diameter and 500~1000 μm in length. Microstructures and chemical compositions of the phases present in the annealed ingots were examined by a JEOL 7100F scanning electron microscope (SEM) equipped with a JEOL energy-dispersive X-ray spectrometer (EDS). γ' solvus temperatures were measured by differential scanning calorimetry (DSC) at a heating rate of 10 °C/min under an Ar gas flow.

Specimens with dimensions of $1.8 \times 1.8 \times 5$ mm^3 were cut from the annealed ingots by electro-discharge machining. The compression axis was set parallel to the thickness direction of the button ingots. Their surfaces were mechanically polished first with SiC paper and then electrolytically in a solution of perchloric acid, butanol and methanol (1:6:12 by volume) at - 40 °C and 18 V. Compression tests were conducted on an Instron-type testing machine from room temperature to 1000 °C in vacuum ($<10^{-3}$ Pa) at a strain rate of 1×10^{-4} s^{-1}. Deformation markings on the specimen surface were examined by optical microscopy to determine the operative slip systems through trace analysis on two orthogonal side faces with additional crystallographic information obtained by electron backscattered diffraction (EBSD) in the SEM. Dislocation structures were examined using a JEM-2000FX transmission electron microscope (TEM) operated at 200 kV with thin foils cut parallel to the {111} macroscopic slip planes from coarse grains. Thin foils for TEM observations were obtained with the above-described solution at - 30 °C and 18 V.

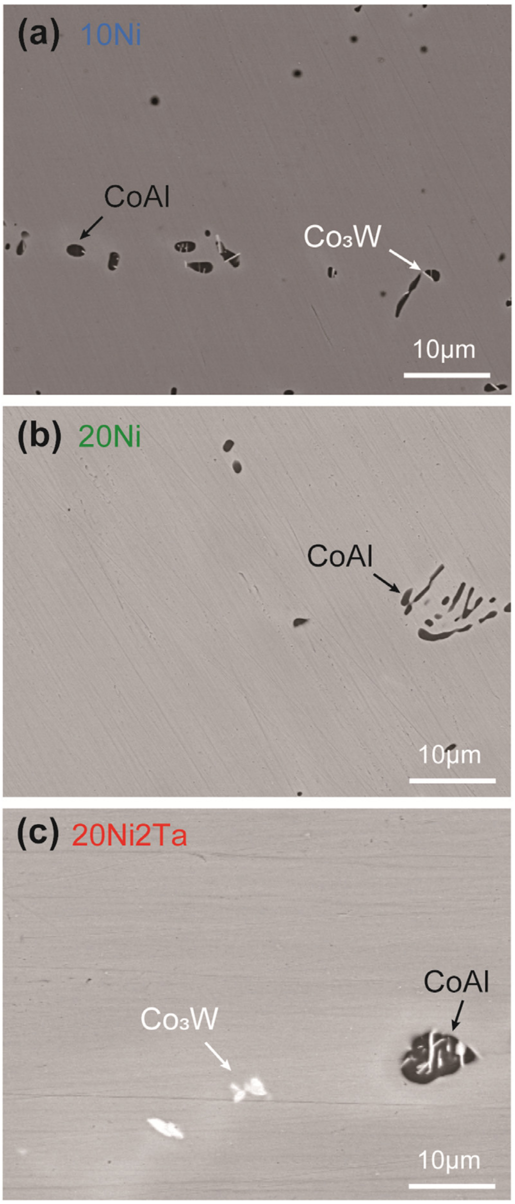

Fig. 1. Typical SEM BSE images of microstructures of (a) 10Ni, (b)20Ni and (c) 20Ni-2Ta alloys after annealing at 850 °C for 168 h. Some minor phases identified are indicated in each of the figures.

3. Results

3.1. Microstructures

Fig. 1(a)–(c) show typical SEM backscattered electron (BSE) images of microstructures of the 10Ni, 20Ni and 20Ni-2Ta alloys, respectively. Although a small amount of additional phases such as CoAl and $Co_3W$are observed (never exceeding 8% by volume), the major phase is γ' ($L1_2$–$Co_3(Al,W)$) for all three alloys. The total volume fraction of additional phases is particularly small for the 20Ni alloy; the volume fractions of the CoAl and Co_3W phases in average are 6.2 and 0.2% for the 10Ni alloy, 2.2 and 0% for the 20Ni alloy and 7.4 and 0.5% for the 20Ni2Ta alloy, respectively. Chemical compositions of the γ' phase in the three alloys measured by EDS are listed in Table 1. Compositions of the γ' phase are close to the alloy nominal compositions as listed in Table 1.

Table 1
Compositions of the γ' phase in the three alloys investigated.

at.%	Co	Al	W	Ni	Ta
10Ni	70.8	9.4	11.7	8.1	–
20Ni	63.4	9.4	11.7	15.5	–
20Ni-2Ta	62.6	9.9	10.2	15.5	1.8

3.2. γ' solvus temperature

Fig. 2(b)–(d) show DSC curves of the 10Ni, 20Ni and 20Ni-2Ta alloys respectively. The DSC curve of the ternary $L1_2$–Co_3(Al,W) base compound (Co-12 at%Al-11 at.%W) [25] is presented in Fig. 2(a) for comparison. The γ' solvus temperature is defined as the endothermic peak temperature as indicated by arrows in Fig. 2, and these are determined to be 1084, 1094 and 1113 °C for the 10Ni, 20Ni and 20Ni-2Ta alloys, respectively. All three alloys have higher γ' solvus temperatures as compared of the ternary $L1_2$–Co_3(Al,W) compound (1061 °C) [25]. The increase of the γ' solvus temperature scales with the amount of the Ni and Ta additions. This is consistent with previous reports [27,29–31] on the beneficial effects of Ni and Ta on γ' solvus temperatures. A similar trend is observed also for the temperature above which the FCC phase starts to precipitate in the γ'phase, as indicated by double-arrows in Fig. 2 (the starting temperature for the endothermic reaction). That temperature is called 'γ' dissolving temperature' hereafter throughout this paper, as the temperature is very important when discussing the high temperature strength. These γ' dissolving temperatures were determined to be 983, 1020 and 1040 °C for the 10Ni, 20Ni and 20Ni-2Ta alloys, respectively. The extent of the increase in the γ' solvus temperature depends, however, on chemical compositions of the base compounds to which alloying additions are made. For example, while the increase in the γ' solvus temperature is 23 °C when 10 at.%Ni is added to the ternary $L1_2$ base compound (Co-12 at%Al-11 at.%W), it is only 10 °C when another 10 at.%Ni is added. Moreover, while the increase in the γ' solvus temperature upon adding 2 at.% Ta is reported to be more than 100 °C for the ternary $L1_2$ base compound [27], it is only 19 °C when Ta is added to the base alloy with 20 at.%Ni.

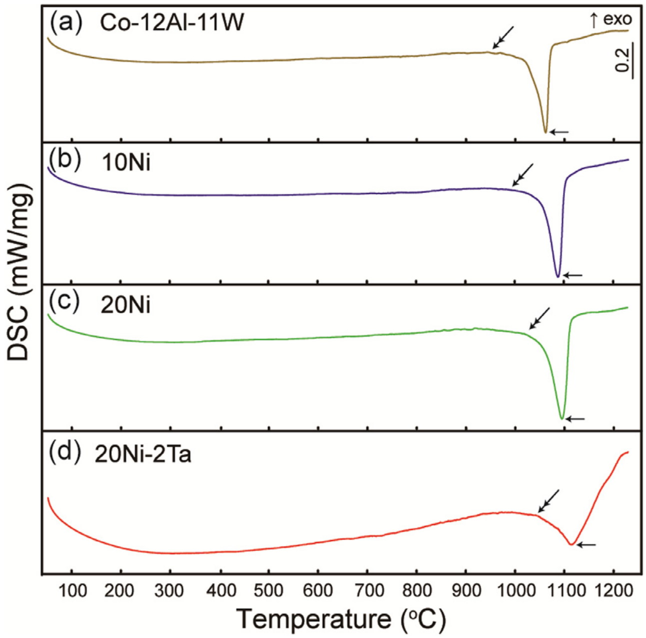

Fig. 2. DSC curves of (a) the ternary $L1_2$-Co_3(Al,W) compound (Co-12 at%Al-11 at.%W), (b) 10Ni, (c) 20Ni and (d) 20Ni-2Ta alloys respectively. The γ' solvus temperature is defined as the endothermic peak temperature (indicated by arrows), while the γ' dissolving temperature is defined as the staring temperature of the endothermic reaction (indicated by double-arrows).

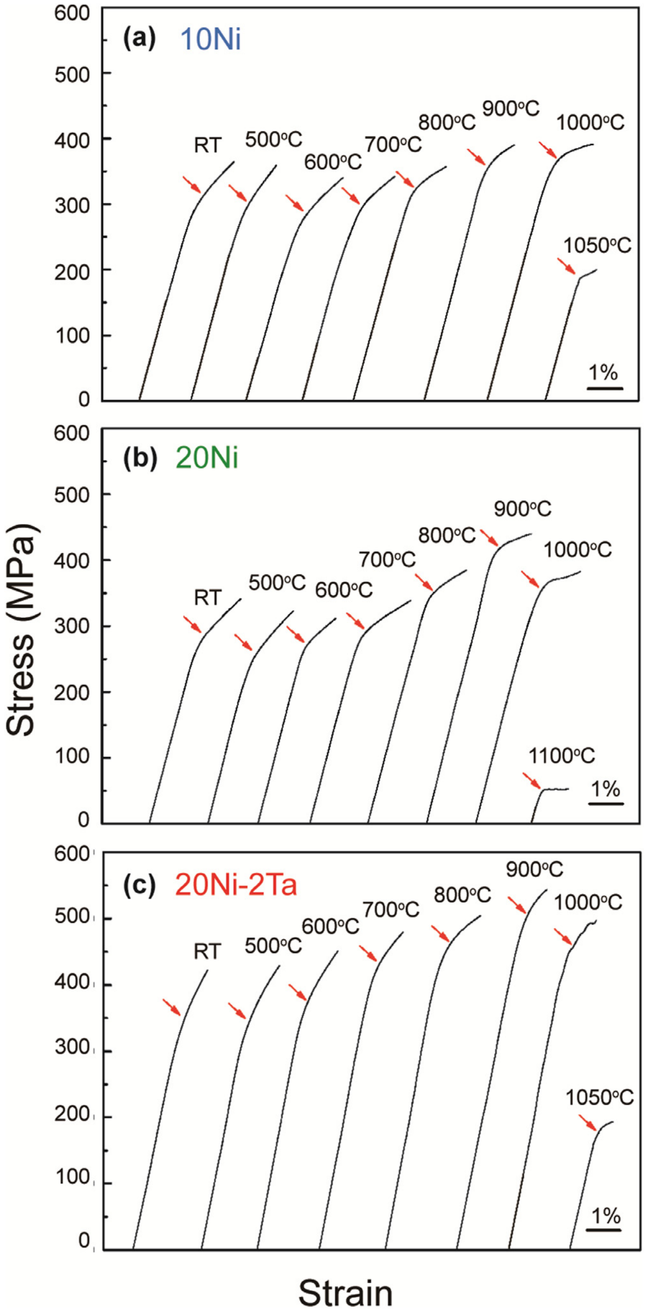

Fig. 3. Selected strain-stress curves of (a) 10Ni, (b) 20Ni and (c) 20Ni-2Ta alloys obtained in compression at temperatures indicated. Yield stress is defined as 0.2% offset stress as marked by arrows.

3.3. Compression deformation

3.3.1. Strain-stress behavior and temperature dependence of yield stress

Fig. 3(a)–(c) show strain-stress curves of the 10Ni, 20Ni and 20Ni-2Ta alloys at some selected temperatures, respectively. The elastic to plastic transition occurs smoothly in general for all these alloys, and therefore a yield stress is defined using the classical 0.2% offset stress criterion (positions marked by arrows in Fig. 3). These yield stresses are plotted in Fig. 4 as a function of temper-

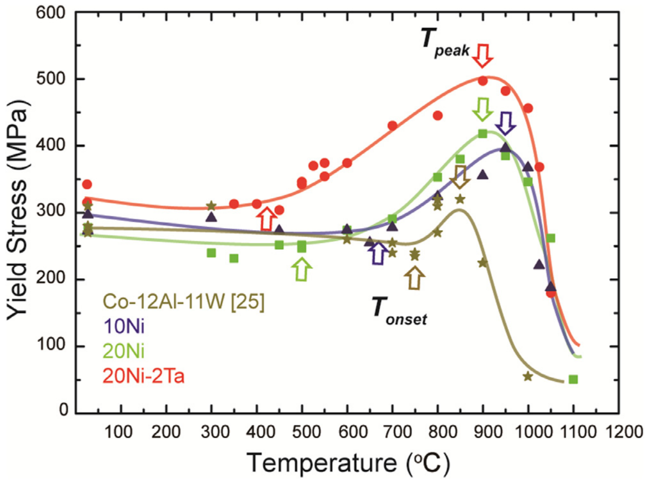

Fig. 4. Temperature dependence of yield stress for the ternary $L1_2$-Co_3(Al,W) compound (Co-12 at%Al-11 at.%W) and the 10Ni, 20Ni and 20Ni-2Ta alloys. Allows pointing upward and downward indicate the boundary between the low and intermediated temperature regimes and that between the intermediated and high temperature regimes, respectively. The former corresponds to the onset temperature of yield stress anomaly.

ature for all three alloys, together with those for the ternary base $L1_2$ compound (Co-12 at%Al-11 at.%W) [25]. The data points plotted in Fig. 4 were all obtained from individual specimens, and a small experimental scatter is apparent. All three alloys show the same general trend. At low temperatures yield stresses stay almost constant and decreases only little with increasing temperature. Then, there is an increase towards a stress maximum in the intermediate temperature regime which is followed by a sharp decrease in the high temperature regime. Arrows pointing up and down in Fig. 4 indicate the transitions between the low and intermediate (upward arrows) and the intermediate and high temperature regimes (downward arrows). The yield stress anomaly apparent in Fig. 4 is in the focus of the present paper. The elementary processes which are responsible for this anomaly will be studied using transmission electron microscopy (TEM), as will be described in the forthcoming sections. We keep in mind that Fig. 4 shows that the YSA-onset (650±50, 500±50 and 400±50 °C, respectively) for the 10Ni, 20Ni and 20Ni-2Ta alloys are 150, 300 and 400 °C lower than what was observed for the ternary $L1_2$ base compound (800±50 °C). Throughout the present paper, the onset of the yield stress anomaly will be referred to as YSA-onset. The extent of this decrease in onset temperatures of the yield stress anomaly is directly related to the increase in the thermodynamic stability of the γ' phase, i.e., the increase in the γ' solvus temperature.

The boundary between the intermediate and high temperature regimes is defined as the peak temperature in Fig. 4, and the peak temperature is also observed to increase by 100–150 °C upon alloying with Ni and Ta. The increase in the peak temperature, however, is the largest for the 10 Ni alloy, and its extent is not consistent with the increase in the γ' dissolving temperature for the three alloys. This will receive attention in the next section, to clarify this phenomenon is another scientific objective of the present paper. As compared to the ternary $L1_2$ base compound, the three alloys 10Ni, 20Ni and 20Ni-2Ta show a lower YSA-onset and increased peak temperatures. They show a larger intermediate temperature regime of yield stress anomaly, and thereby improving the intermediate and high temperature strength quite drastically.

3.3.2. Deformation markings

Fig. 5 shows deformation markings observed on a side surface of the 10Ni, 20Ni and 20Ni-2Ta specimens deformed at temperatures indicated next to each micrograph. The trace analysis results for the activated slip planes are also indicated in each figure, together with stereographic projections of crystal orientations of all grains analysed. For all three alloys, {111} planes are the only the activated slip planes below the peak temperature, independent of the crystal orientation (Fig. 5(a),(d),(g)). {111} type of planes are found to be the only the activated slip planes also for the temperature regime above the peak temperature (Fig. 5(b),(c),(e),(f),(h),(i)), unlike in many other $L1_2$ intermetallic compounds such as Ni_3Al, in which {010} cube slip is usually found to be activated except for some limited orientations close to [001]. It is important to note that the dominant activation of {111} slip planes is observed below (Fig. 5(b),(e),(h)) and above (Fig. 5(c),(f),(i)) the γ' dissolving temperature for all three alloys. This indicates that although the yield stress maximum is considered to correspond to the γ' dissolving temperature for the ternary $L1_2$ base compound [25], the activation of the {111} slip planes above the peak temperature is not related to the appearance of the disordered FCC phase but is an inherent property of the $L1_2$–Co_3(Al,W) compounds. This will be discussed in detail later in Section 4.3.

3.3.3. Dislocation structures

Fig. 6 shows TEM dislocation structures observed in the 10Ni, 20Ni and 20Ni-2Ta alloys deformed at temperatures below (Fig. 6(a), (c), (e)) and above (Fig. 6(b), (d), (f)) the YSA-onset, as the deformation temperature is indicated in each of the figures. All thin foils were cut parallel to the (111) macroscopic slip plane, and the YSA-onset were judged by the extent of alignment of dislocations parallel to their screw orientations (by bright-field (BF) image as shown in Fig. 6) and the occurrence of cube cross-slip of screw dislocations (by weak-beam dark-field WBDF imaging as shown in Figs. 7 and 8), both of which are well-known characteristics for dislocation structures in the anomalous temperature regime in many $L1_2$ compounds [36,37,42,43], including Co_3(Al,W) [25]. Most dislocations imaged in Fig. 6 are those with **b** (Burgers vector)=$[\bar{1}01]$ gliding on (111) for all the three alloys. While these dislocations are in general curved smoothly without preferred orientations on their slip plane at low temperature (i.e., below the YSA-onset) (Fig. 6(a), (c), (e)), the extent of alignment of dislocations along their screw orientation becomes significant in the BF-TEM images in the anomalous temperature regime where the yield stress increases anomalously with temperature (Fig. 6(b), (d), (f)). The YSA-onset thus determined by TEM observations coincides with those determined from the yield stress-temperature curves of Fig. 4.

Low-magnification TEM images of dislocations with $\boldsymbol{b}=[\bar{1}01]$ gliding on (111) observed in the 10Ni, 20 Ni and 20Ni2Ta alloys deformed respectively at 750, 600 and 600 °C in the anomalous temperature regime are shown in Fig. 7(a), (d) and (g). For all three alloys, the dislocations are observed to dissociate into two superpartial dislocations with $\boldsymbol{b} = 1/2[\bar{1}01]$ separated by an anti-phase boundary (APB) with a general tendency to align along the screw orientation, and these screw segments are observed to be connected with each other by a superkink that contains edge components. Tilting analysis made for a different dislocation with $\boldsymbol{b}=[\bar{1}01]$ in the same foil of the 10Ni alloy indicates that the APB limited by the two coupled superpartials with $\boldsymbol{b} = 1/2[\bar{1}01]$ lies mostly on the (010) cube cross-slip plane as opposed to the (111) glide plane. The separation distance for the coupled superpartials is observed to be the widest along the [010] zone-axis (Fig. 8). Essentially, the same dislocation configurations are observed in the 20Ni and 20Ni2Ta alloy (Fig. 7(d) and (g)). This clearly indicates that thermally-activated cube cross-slip of $1/2[\bar{1}01]$ superpartial dislocations is responsible for YSA for Co_3(Al,W) compounds as in many other $L1_2$ compounds [36,37,44–46]. For all the 10 Ni, 20 Ni and 20Ni2Ta alloys, two-fold dissociation of the $[\bar{1}01]$ disloca-

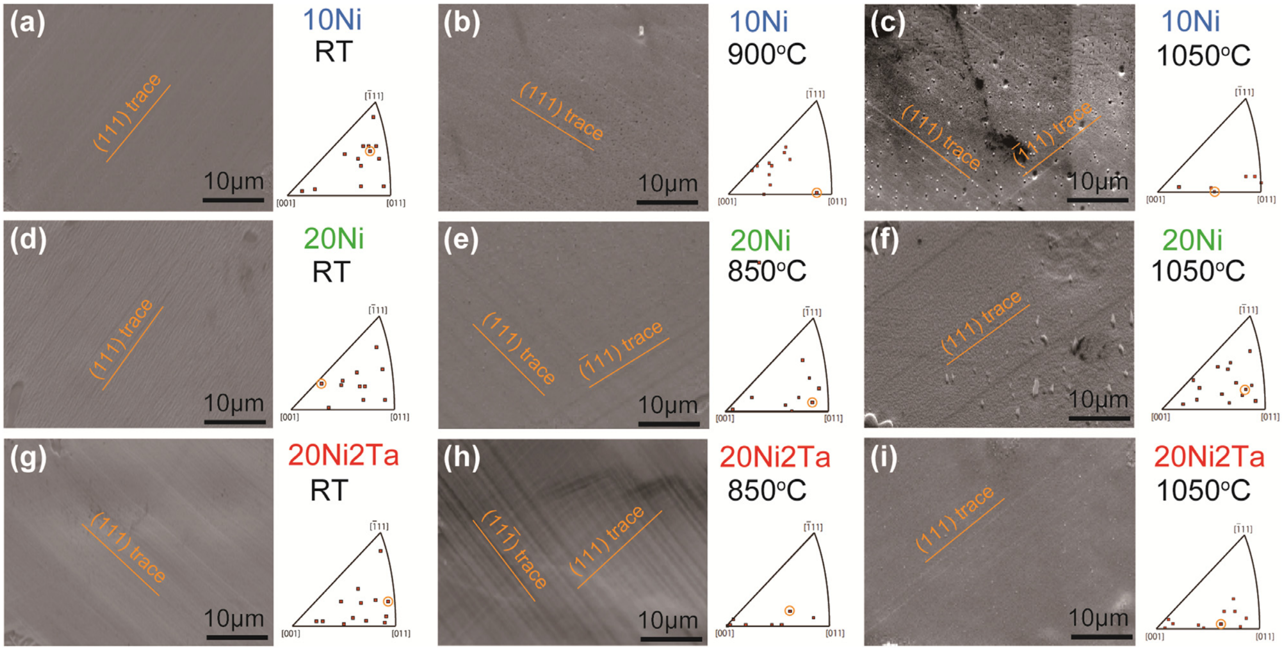

Fig. 5. Deformation markings observed on a side surface of (a)–(c) 10Ni, (d)–(f) 20Ni and (g)–(i) 20Ni-2Ta alloys deformed at temperatures indicated in each of the figures. The results of trace analysis for the activated slip plane are also indicated in each of the figures, together with stereographic projections of crystal orientations of grains analysed. The crystal orientation of the grain of the figure are marked with a circle in the stereographic projection.

Table 2
The APB energies on (111) and (010), APB energy anisotropy parameter (λ), activation enthalpy (*H*) for thermally-activated cross slip of super-partial dislocations from (111) to (010), CSF energy and base strength of ternary base, 10Ni, 20Ni and 20Ni2Ta alloys.

	$\gamma_{APB(111)}$ (mJ/m^2)	$\gamma_{APB(010)}$ (mJ/m^2)	λ	γ_{CSF} (mJ/m^2)	H (kJ/mol)	Base strength (MPa)
Ternary [25]	153	139	0.91	137	135	240
10Ni	160	145	0.90	163	117	260
20Ni	169	156	0.89	183	104	235
20Ni2Ta	246	194	0.79	199	91	290

tion is also observed along superkinks without any evidence of further sub-dissociation of each of the coupled $1/2[\bar{1}01]$ superpartials into two Shockley partials with $\boldsymbol{b}$ = 1/6<112>, as shown in the enlargement of the framed areas in Fig. 7(b), (e) and (h). This differs from what is observed in the ternary Co_3(Al,W) base compound, in which four-fold dissociation involving these four super-Shockley partials is clearly observed along superkinks [25], indicating that the energy of a CSF bounded by two super-Shockley partials with $\boldsymbol{b}$ = 1/6<112> is fairly increased by additions of Ni and Ta to Co_3(Al,W).

The APB energies on (111) ($\gamma_{APB(111)}$) for the three alloys were estimated by measuring the dissociation widths along the superkink with edge components as a function of the angle θ between the Burgers vector and line vector (Fig. 9(a)–(c)), while those on (010) ($\gamma_{APB(010)}$) were estimated by measuring the dissociation width along the screw dislocation (7.1, 6.6 and 5.3 nm respectively for the 10 Ni, 20 Ni and 20Ni2Ta alloys). The latter is based on the assumption that the Kear-Wilsdorf lock formed along the screw orientation is of the complete type, in which the APB bounded by two super-partial dislocations with $\boldsymbol{b} = 1/2[\bar{1}01]$ lies exclusively on (010). Indeed, the ratio of the dissociation width projected along [010] to that projected along [111] was close to the 1.74, expected for the complete Kear-Wilsdorf lock for all three alloys (Figs. 7 and 8). In the calculation of APB energies on (111) and (010), we used the shear modulus (101 GPa) for the ternary base Co_3(Al,W) compound [15], as we have not measured elastic constants for any of 10 Ni, 20 Ni and 20Ni2Ta alloys. The results of calculations are tabulated in Table 2. As we expected, the APB energy on (111) increases by alloying with Ni and Ta in the order of 10 Ni < 20 Ni < 20Ni2Ta. This is also the case for the APB energy on (010). This is exactly what we expect: The increased APB energy upon alloying with Ni and Ta is coupled to the stabilizing effect of these elements on the γ' phase.

4. Discussion

In our previous study on polycrystals of ternary Co_3(Al,W) with the $L1_2$ structure (Co-12 at%Al-11 at.%W) [25], we have shown that the intermediate-temperature strength of this ternary $L1_2$ base compound is low as the YSA-onset is as high as 700 °C and that the high-temperature strength is also low with the low peak stress temperature as the γ' phase is easily destabilized due to the low γ' solvus temperature (~1060 °C). Thermally-activated cross slip of $1/2[\bar{1}01]$ superpartial dislocations from (111) to (010) planes is identified to be responsible for YSA in ternary Co_3(Al,W) as in many other $L1_2$ compounds such as Ni_3Al, but the low CSF energy is supposed to lead to the high YSA-onset in ternary Co_3(Al,W) [25]. In the present study, however, both the intermediate- and high-temperature strengths of the $L1_2$–Co_3(Al,W) compound are significantly increased by alloying with Ni and Ta, both of which are known as the γ'-phase stabilizer, through increasing the YSA-onset and the peak stress temperature, respectively (Fig. 4). We believe that both the increased intermediate- and high-temperature strengths of $L1_2$–Co_3(Al,W) contribute to the improved creep strength of Co-based alloys upon alloying with these γ'-phase stabilizing elements [7,9,11,14,27,41]. We thus discuss in the follow-

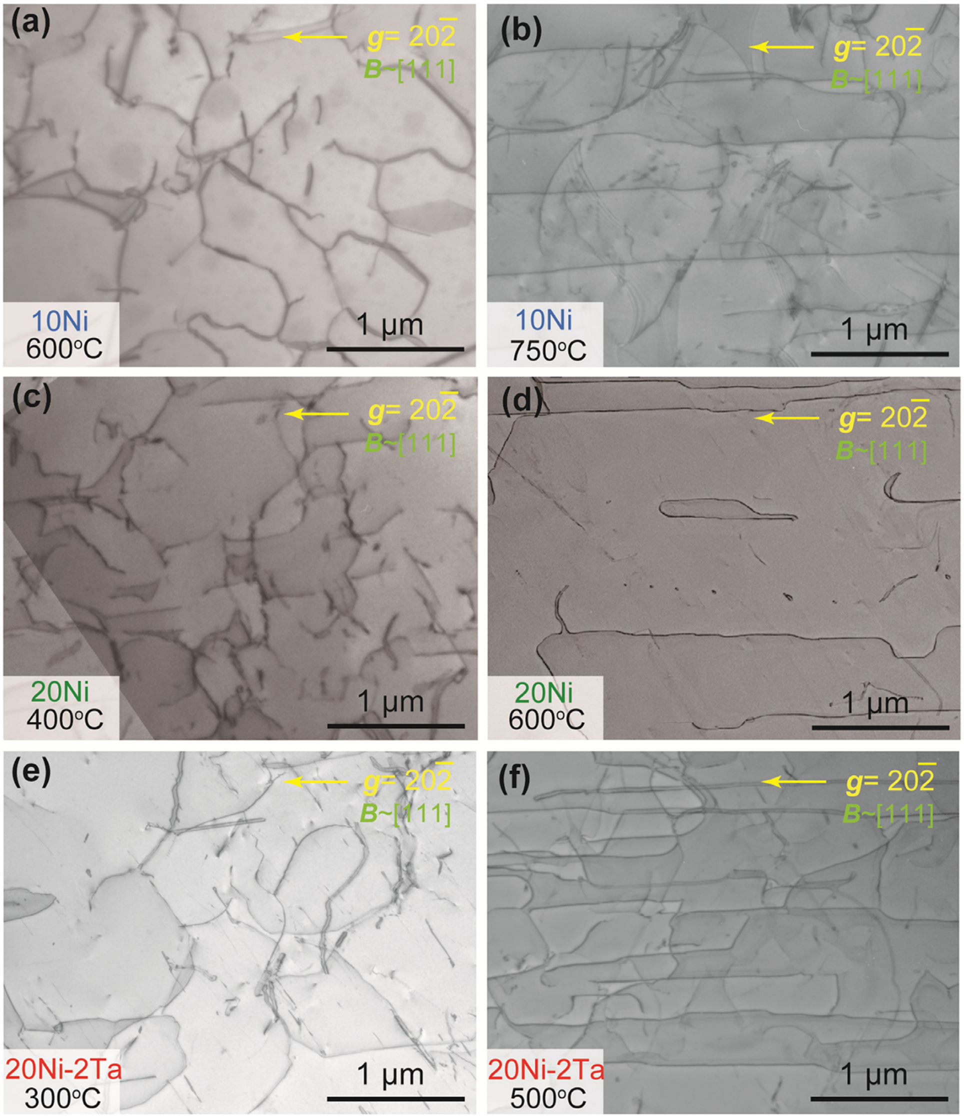

Fig. 6. TEM dislocation structures observed in (a),(b) 10Ni, (c),(d) 20Ni and (e),(f) 20Ni-2Ta alloys deformed at temperatures below ((a), (c), (e)) and above ((b), (d), (f)) the onset temperature for yield stress anomaly. All thin foils were cut parallel to the (111) macroscopic slip plane.

ing the possible reasons for the improved intermediate- and high-temperature strengths of the $L1_2$ compound itself.

4.1. Improved intermediate-temperature strength; reduced YSA-onset

As seen in Fig. 4, the increased intermediate-temperature strength of $L1_2$–$Co_3(Al,W)$ is due to the decreased YSA-onset upon alloying with Ni and Ta. The YSA-onset decreases more significantly as the amount of additions for these γ'-phase stabilizing elements (Ni and Ta) increases. In many $L1_2$ compounds, yield stress anomaly is known to occur by thermally-activated cross slip of superpartial dislocations with $\boldsymbol{b} = 1/2[\bar{1}01]$ from (111) to (010), and this is confirmed also for the ternary $L1_2$–$Co_3(Al,W)$ base compound [25] and for Ni- and Ta-added $L1_2$–$Co_3(Al,W)$ compounds in the present study. Cross slip of the superpartial dislocation with $\boldsymbol{b} = 1/2[\bar{1}01]$ in $L1_2$ compounds can be considered similarly to that of the perfect dislocation with $\boldsymbol{b} = 1/2[\bar{1}01]$ in fcc metals. This is due to the fact that the $L1_2$ structure is a superlattice structure based on the fcc structure, although the planar fault bounded by two super-Shockley partial dislocations with $\boldsymbol{b} = 1/6<112>$ in the $L1_2$ structure is not a simple stacking fault as in the fcc structure but is CSF that accompanies not only with a fault in stacking of {111} atomic planes but also with a fault in atomic bonding between like and unlike atoms. The energy to form a constriction (W_c: constriction energy) is needed for the perfect dislocation to cross slip in fcc metals, as formulated by Stroh [47,48].

$$W_c = \frac{\mu b^2 d}{30}\left[\ln\left(\frac{d}{b}\right)\right]^{\frac{1}{2}}, \tag{1}$$

where d is the separation distance of Shockley partial dislocations along the screw orientation and b is the magnitude of the Burgers vector of the perfect dislocation with $\boldsymbol{b} = 1/2[\bar{1}01]$. The separation distance of partial dislocations (d) along the screw orientation can be calculated as a function of the stacking fault energy (γ_{SF}) (the CSF energy (γ_{CSF}) in the case of the $L1_2$ structure) in the isotropic elasticity approximation with the following equation.

$$d = \frac{\mu b_p^2}{8\pi\gamma_{SF}}\frac{2-3\nu}{1-\nu} \tag{2}$$

where μ is shear modulus, ν is Poisson's ratio and b_p is the magnitude of the Burgers vector of the Shockley partial dislocation. The frequency (q) for thermally-activated cross slip of the perfect dislocation is then described with the usual Arrhenius-type equation,

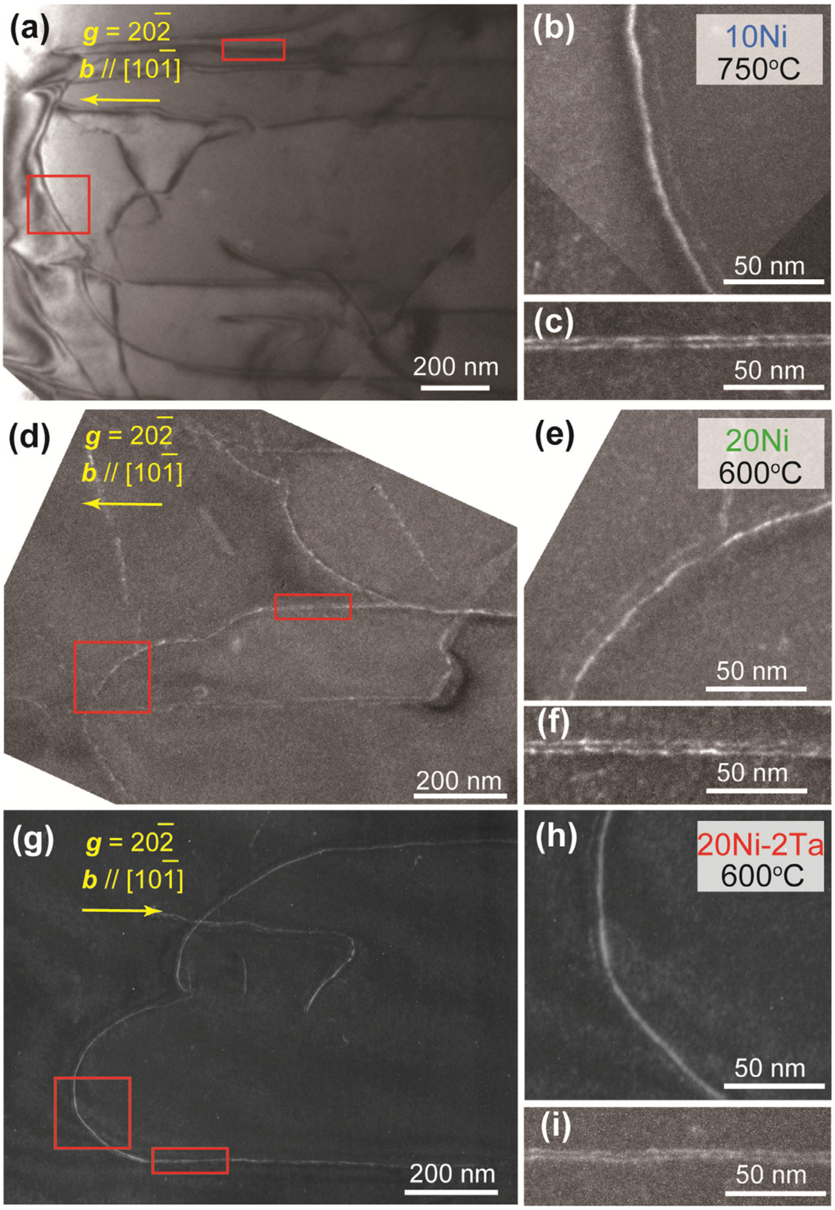

Fig. 7. Low-magnification TEM images of dislocations with $\boldsymbol{b}=[\bar{1}01]$ gliding on (111) observed in (a) 10Ni, (d) 20 Ni and (g) 20Ni2Ta alloys deformed respectively at 750, 600 and 600 °C in the anomalous temperature regime. The enlargements of the framed areas in (a), (d) and (g) are shown in (b) and (c), (e) and (f), and (h) and (i), respectively.

as follows.

$$q = q_0 \exp\left[-\frac{W_c}{kT}\right] \tag{3}$$

where q_0 is the pre-exponential factor of the order of 10^{13} s^{-1}, k is the Boltzmann constant and T is absolute temperature. Fig. 10(a) shows the temperature-dependent frequency for cross-slip in L1$_2$–Co$_3$(Al,W) calculated as a function of CSF energy with the reported values of shear modulus (μ=101 GPa) and Poissson' ration (ν=0.289) for the ternary L1$_2$ base compound [15]. The onset temperature for cross slip tends to increase quite significantly with the decrease in the CSF energy due to the increased constriction energy when the CSF energy changes from 200 to 140 mJ/m^2.

Paidar, Pope and Vitek (PPV) [49] deduced the activation enthalpy (H) for thermally-activated cross slip of superpartial dislocations with $\boldsymbol{b}$ = 1/2[$\bar{1}$01] from (111) to (010) to give rise to yield stress anomaly in L1$_2$ compounds, incorporating the energy of two constrictions formed on the superpartials, the self-energy of the double kink, the energy gain of the dislocation due to the anisotropy of APB energy, the energy of cross-slip derived by the stress component on the cross-slip plane and the interaction energy between two kinks. Later, Yoo [50] pointed out that cube cross slip is promoted also by torque force acting on the coupled superpartials with $\boldsymbol{b}$ = 1/2[$\bar{1}$01] arising from the elastic anisotropy (that is usually expressed as $A = 2C_{44}/(C_{11}-C_{12})$ with single-crystal elastic stiffness constants C_{ij}). Hirsh [48] subsequently re-wrote the activation enthalpy in a way slightly different from the formulation by PPV [49], incorporating the torque force effect in the term for the energy of cross-slip derived by the stress component on the cross-slip plane and assuming a double jog mechanism for cube cross-slip as follows.

$$H = 2W_c + \frac{\mu b^2}{2\pi(1-\nu)}\left[\ln\left(\frac{2w}{eb}\right) - (1-\nu)\right] + \frac{\mu b^2 w}{4\pi} - 2F_{AC} w l_c \tag{4}$$

The first term is the energy of constrictions as calculated by (1), the second term is the self-energy of the two jogs of height w

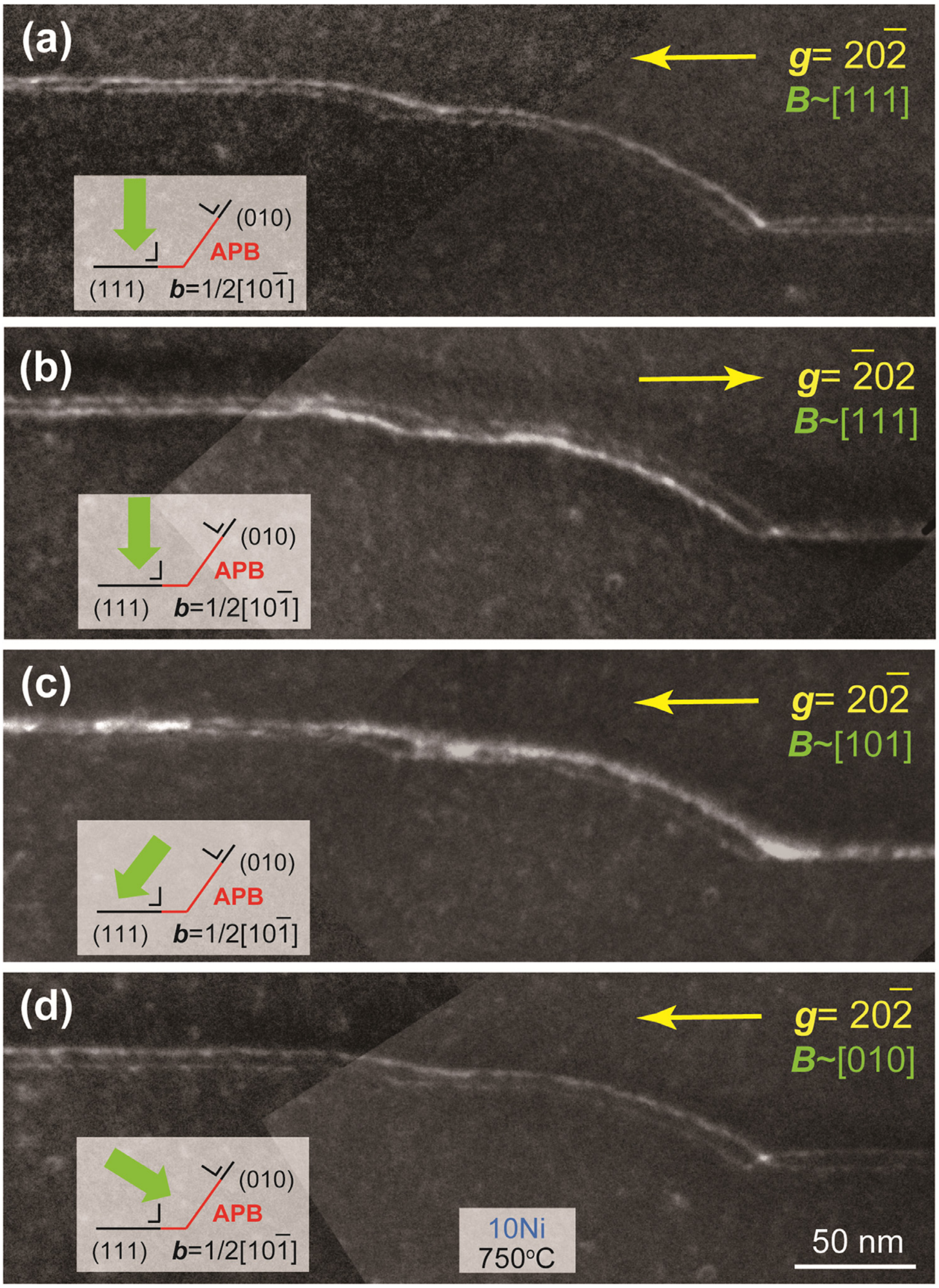

Fig. 8. Tilting analysis of a dislocation with ***b***=[$\bar{1}01$] gliding on (111) observed in the 10Ni alloy deformed at 750 °C. The zone-axis orientations (**B**) used imaging are indicated in each of the figures.

(usually taken as $b/2$), the third is the core energy estimate, and the forth term is the combined expression for the work done by the effective stress on (010) and the interaction energy between the two jogs. F_{AC} is the force on the leading partial on the (010) plane as expressed with

$$F_{AC} = E\gamma_{APB(111)} + \tau_{(010)}b - \gamma_{APB(010)} \tag{5}$$

with

$$E = \frac{A\cos\varphi\sin\varphi}{\sin\varphi[(A-1)\cos^2\varphi + 1]} \tag{6}$$

where $\tau_{(010)}$is the resolved shear stress on (010). E is calculated to be 1.061 with φ(angle between (111) and (010))=54°44′ and $A = 3.26$ for the ternary base alloy [15]. We used the same value for the elastic anisotropy parameter ($A = 3.26$) for all three alloys containing Ni and Ta, as we have not measured elastic constants for any of the three alloys. As the resolved shear stress on (111) ($\tau_{(111)}$) and $\tau_{(010)}$ is approxomated as $\tau_{(010)} \approx 0.8\tau_{(111)}$ for orientations near the center of the streographic triangle, the Eq. (5) can be written as,

$$F_{AC} = 1.061\gamma_{APB(111)} - \gamma_{APB(010)} + 0.8\tau_{(111)}b = \gamma_{APB(111)}(1.061 - \lambda) + 0.8\tau_{(111)}b \tag{7}$$

where λ is the APB energy anisotropy factor defined as $\lambda = \gamma_{APB(010)}/\gamma_{APB(111)}$. l_c in (4) is the critical length of double jog as expressed with

$$l_c = \frac{1}{2}\left(\frac{\mu b^2 w}{\pi F_{AC}}\right)^{1/2} \tag{8}$$

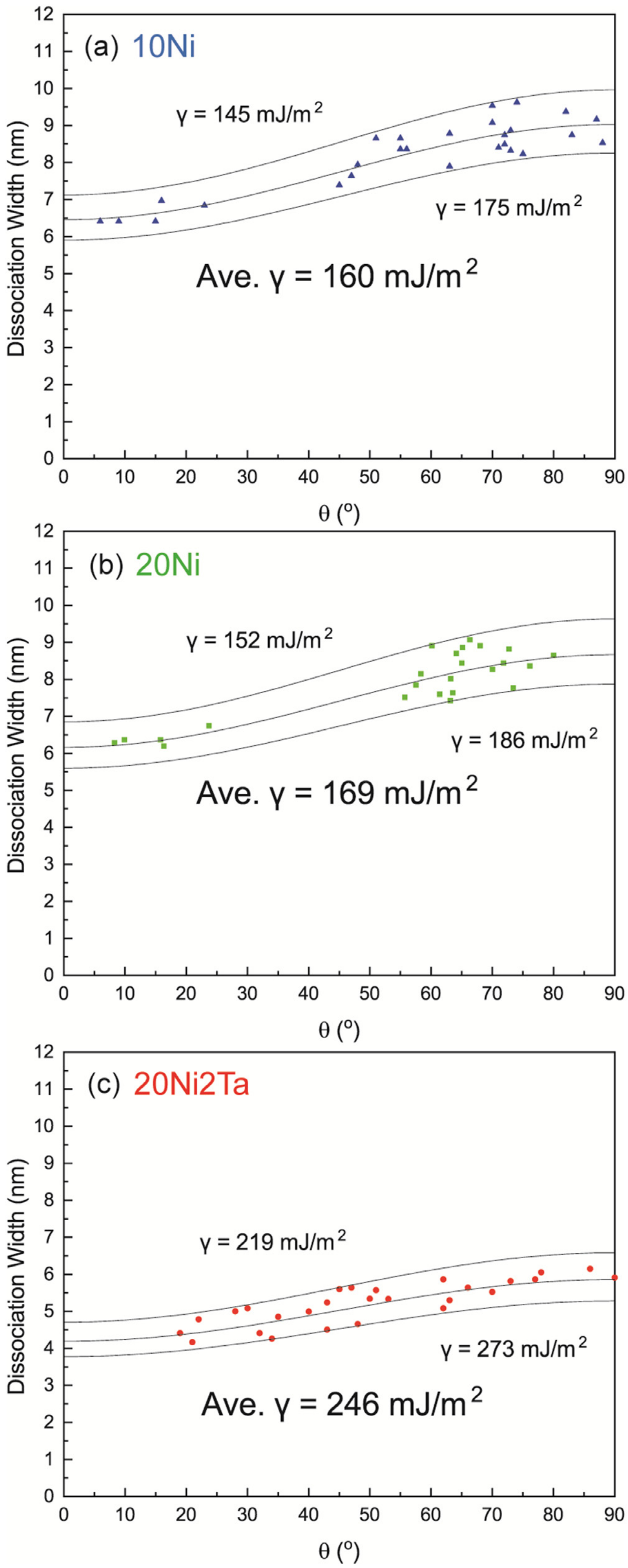

Fig. 9. Dissociation width between two coupled super-partial dislocations with $\boldsymbol{b}$ = 1/2[$\bar{1}$01] measured along superkinks on (111) as a function of the angle θ between the Burgers vector and line vector for (a) 10Ni, (b) 20 Ni and (c) 20Ni2Ta alloys deformed respectively at 750, 600 and 600 °C in the anomalous temperature regime.

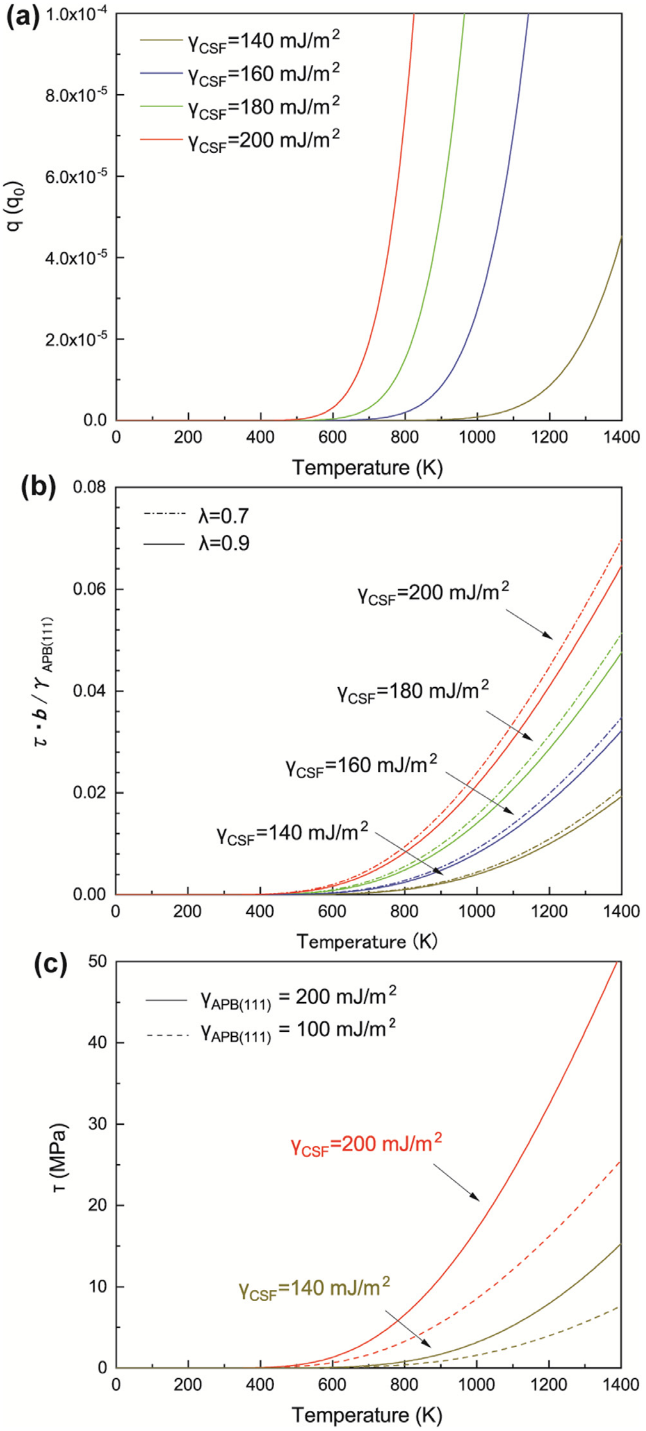

Fig. 10. (a) Temperature-dependent frequency for cross-slip in L1$_2$–Co$_3$(Al,W) calculated as a function of CSF energy. (b) Temperature dependence of the normalized resolved shear stress on (111) ($\tau_{(111)}b/\gamma_{APB(111)}$) in L1$_2$-Co$_3$(Al,W) calculated as a function of CSF energy with two different λ values (0.7 and 0.9) for the APB energy anisotropy. (c) Temperature dependence of resolved shear stress on (111) ($\tau_{(111)}$) in L1$_2$-Co$_3$(Al,W) calculated as a function of CSF energy and the APB energy on (111) with a fixed APB energy anisotropy (λ=*0.9*).

Then, the activation enthalpy (H) for thermally-activated cross slip of super-partial dislocations from (111) to (010) can be calculated with the use of the Eqs. (1), (7), (8) and appropriate numerical values. The elastic energy (second) term becomes negative for $w/b < 2$ and is taken to be zero as in [48]. The 'work' (fourth) term is found to be insensitive to $\tau_{(111)}$, as it is calculated to be 11.0,

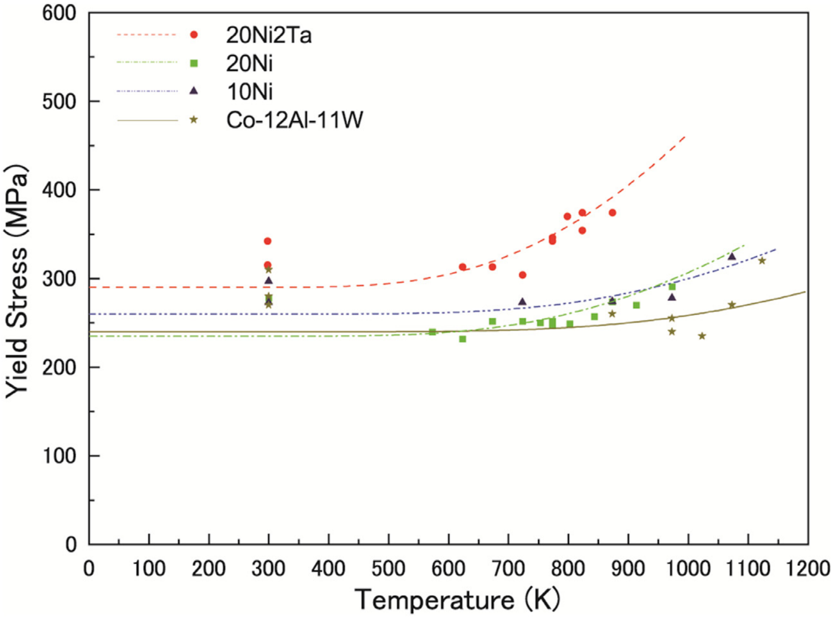

Fig. 11. Comparison of the calculated temperature dependence of yield stress with experimental results for the ternary base and 10Ni, 20Ni and 20Ni2Ta alloys.

12.1 and 13.0 kJ/mol respectively for $\tau_{(111)}$=40, 125 and 200 MPa for $\gamma_{APB(111)}$=200 mJ/m^2 and $\lambda = 0.8$. We thus use a fixed value of $\tau_{(111)}$=40 MPa for the activation energy calculation. Then, the resolved shear stress on (111) plane ($\tau_{(111)}$) can be expressed with H in (4) as [49],

$$\frac{\tau_{(111)} b}{\gamma_{APB(111)}} = C \exp\left(\frac{-H}{3kT}\right) \tag{6}$$

where C is a constant (suggested to be close to unity [49]). We calculate the temperature dependence of the normalized resolved shear stress on (111) ($\tau_{(111)} b/\gamma_{APB(111)}$) in Fig. 10(b) to see how the CSF energy and APB energy anisotropy affect the onset temperature and temperature variation of yield stress anomaly in L1$_2$–Co$_3$(Al,W) with the use of $C = 1$. Fig. 10(b) clearly indicates that the YSA-onset decreases as the CSF energy increases so as to increase the intermediate-temperature strength rather significantly but that the magnitude of yield stress anomaly does not much depend on the APB energy anisotropy (in the range of λ= 0.7∼0.9) for a given CSF energy when the stress is expressed with the normalized resolved shear stress on (111) ($\tau_{(111)} b/\gamma_{APB(111)}$). The significance of the APB energy on (111) in determining the temperature-dependent strength becomes evident, however, when the resolved shear stress on (111) ($\tau_{(111)}$) is plotted as in Fig. 10(c) instead of the normalized resolved shear stress on (111) ($\tau_{(111)} b/\gamma_{APB(111)}$) as in Fig. 10(b). As the APB energy on (111) increases, the extent of yield stress anomaly (i.e., the increase in the resolved shear stress on (111) with temperature) becomes more significant. On top of that, the base strength (the strength before yield stress anomaly starts to occur) tends to increase with the increase in the APB energy on (111) and the CSF energy, as will be discussed later in detail.

The temperature-dependent yield stresses for the 10Ni, 20 Ni and 20Ni2Ta alloys as well as for the ternary base alloy are calculated in Fig. 11 as the sum of the base strength (the strength before yield stress anomaly starts to occur) and the stress calculated with the Eq. (5) multiplied by a factor of 6 (but not by the Taylor factor of 3.06) referring to our previous study [24,25] with the use of the APB energy on (111), APB energy anisotropy (λ) and the CSF energy tabulated in Table 2. The factor of 6 was found when converting the CRSS value obtained from micropillar compression tests [24] into the bulk polycrystalline yield stress in the ternary compound [25], most probably accounting for the grain size effects. As the specimen preparation method is exactly the same for the ternary base alloy and other three alloys containing Ni and Ta, the grain sizes for all the alloys are indeed very similar. While the APB energy on (111) and APB energy anisotropy (λ) used are those experimentally determined in the present study, the CSF energy that is important to determine the YSA-onset is used as a fitting parameter. As seen in Fig. 11, the temperature-dependent yield stresses for the 10Ni, 20 Ni and 20Ni2Ta alloys as well as for the ternary base alloy are reproduced very well.

4.2. *Improved intermediate-temperature strength; increased L1$_2$ phase stability*

The CSF energies could not be experimentally determined for the 10Ni, 20 Ni and 20Ni2Ta alloys, as the corresponding dissociation widths were below the resolution limit for WBDF-TEM imaging. However, these values could be estimated as a fitting parameter in the calculation of the temperature-dependent yield stresses of Fig. 11. The deduced CSF energies are plotted in Fig. 12(a) as a function of the APB energy on (111) for the ternary base alloy and the 10Ni, 20 Ni and 20Ni2Ta alloys. Obviously, there is a clear correlation between the two; the CSF energy tends to increase with the increase in the APB energy on (111). This is a natural consequence for the increased L1$_2$ phase stability, as can be easily understood from the expression of the APB energy on (111) and CSF energy of the L1$_2$ compound of the A$_3$B-type with pair-wise interactions considering only the first- and second-nearest neighbours as described,

$$\gamma_{APB(111)} = \left(2V^{(1)} - 6V^{(2)}\right)/\sqrt{3}a^2 \tag{7}$$

$$\gamma_{CSF} = \gamma_{APB(111)} + 4\{\phi_{AA}(r') + \phi_{AB}(r')\}/\sqrt{3}a^2 \tag{8}$$

where a is the lattice parameter and $V^{(k)}$ are the k th neighbor ordering energies given as

$$V^{(k)} = \{\phi_{AA}^{(k)} + \phi_{BB}^{(k)} - 2\phi_{AB}^{(k)}\}/2 \tag{9}$$

and $\phi_{ij}^{(k)}$are the pairwise interaction energies between k th neighbor atoms i and j, and $\phi_{ij}(r')$is the interaction energy between

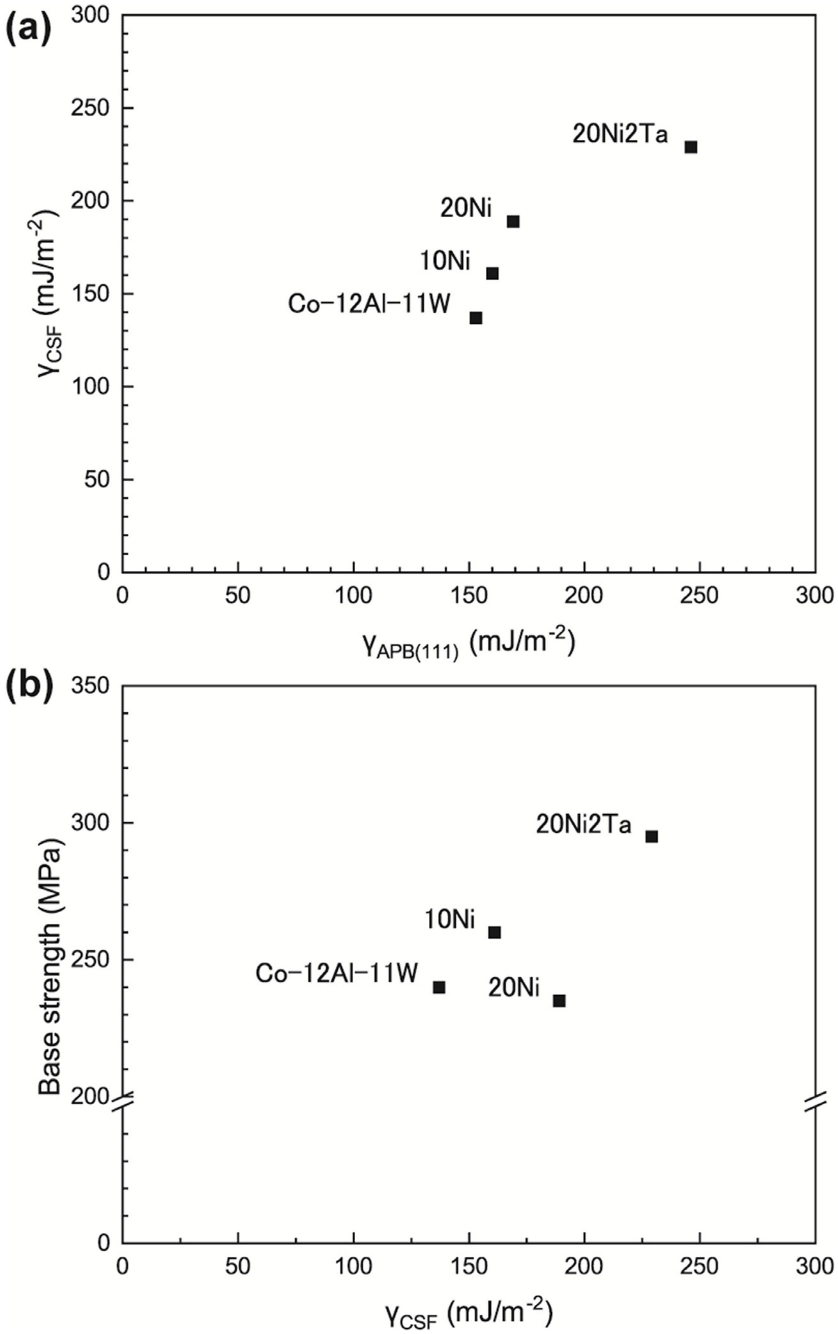

Fig. 12. The relationship (a) between the APB energy on (111) and CSF energy and (b) between the base strength and the CSF energy in the ternary base and 10Ni, 20Ni and 20Ni2Ta alloys.

i and j atoms at the separation $r' = (2/\sqrt{3})a$. Both the APB energy on (111) and the CSF energy of the $L1_2$ compound increase with the increase in the ordering energy, i.e., the phase stability. Of interest to note is that the increase in the APB energy on (111) as well as that in the CSF energy tend to increase both the yield strength at a given temperature (below the peak temperature) and the base strength (that can be defined as the stress before yield stress anomaly occurs) as shown in Fig. 12(b), in which the base strength is plotted as a function of the CSF energy for the ternary base alloy and the 10Ni, 20 Ni and 20Ni2Ta alloys. The base strength of the 20 Ni alloy is exceptionally low. This may be related to microstructure characteristics of the 20 Ni alloy that the volume fraction of the incorporated second and third phases is particularly low (Fig. 1(b)). Indeed, the YSA-onset is low and the extent of yield stress anomaly is high for this alloy (Fig. 4). The increased yield strength at a given temperature with the CSF energy was discussed by Hemker and Mills [51] and subsequently by Caillard and Martin [52] in terms of the increased dislocation exhaustion rate that is promoted with the increase in the CSF energy through frequently occurring cross-slip, leading to higher stress needed to keep a constant strain rate.

The increased $L1_2$ phase stability is thus considered to increase the intermediate-temperature strength of $L1_2$–Co(Al,W) by decreasing the YSA-onset with the increased CSF energy, and by increasing the base strength and the extent of yield stress anomaly (at a given temperature) with the increased APB energy on (111).

4.3. Improved high-temperature strength

In our previous study, the peak temperature is considered to correspond to the γ' dissolving temperature for the ternary L1$_2$ base compound [25]. In the present study, however, the γ' dissolving temperature for the L1$_2$ compound is increased considerably as the phase stability of the L1$_2$ phase is increased by alloying with Ni and Ta, both of which are known as a γ'-stabilizing element. As a result, the peak temperatures for these Ni and Ta added alloys are observed well below the γ' dissolving temperatures, indicating that the peak temperature is not defined by the γ' dissolving temperature. Of interest to note is that {111} slip persists in these Ni and Ta added alloys even above the peak temperatures where the L1$_2$ phase is stable. This is quite different from what is usually observed for Ni$_3$Al-based L1$_2$ compounds, in which {010} slip is observed above the peak temperature except for a narrow orientation range close to <001> [36,37,53]. However, the persistence of {111} slip above the peak temperature is similarly observed for Co$_3$Ti-based L1$_2$ compounds [54–56]. The YSA-onset is known to be far below room temperature for most Ni$_3$Al-based compounds [36,37,57] while it is reported to be as high as 400 °C for Co$_3$Ti-based L1$_2$ compounds [54–56]. As the CSF energy is considered to determine the YSA-onset as we discussed in the previous sections, these two different types of L1$_2$ compounds, Ni$_3$Al- or Co$_3$Ti-based compounds, are supposed to have quite different CSF energies. Although there is no experimental report in the past, Co$_3$Ti-based L1$_2$ compounds are considered to have a relatively low CSF energy as Co$_3$(Al,W)-based L1$_2$ compounds when judged from their high YSA-onset [54–56]. The relatively low CSF energy indicates that each of two super-Shockley partial dislocations (with $\boldsymbol{b} = 1/6<112>$) separated by a CSF possesses a core structure spreading in a planar manner on the (111) glide plane as the Shockley partial dislocation in the fcc structure does, making slip on (010) in a substantially long distance difficult even at high temperatures and leading to the persistent {111} slip above the peak temperature. A study on the dislocation core structure to elucidate this has yet to be done. If this is the case, however, the strength decrease above the peak temperature might result from viscous flow. Then, any alloying elements that reduce the overall atomic diffusivity of the L1$_2$ compound must be effective for further improving the high-temperature strength by increasing the peak temperature.

5. Conclusions

The effects of Ni and Ta additions on the mechanical properties of the L1$_2$ compound Co$_3$(Al,W) have been investigated by compression testing between room temperature and 1000 °C. The results obtained are summarized as follows:

(1) Additions of Ni and Ta result in an increase of both the L1$_2$ solvus temperature and the yield strength at intermediate and high temperatures. The strength increase scales with the amount of additions of these elements and thus with an increasing stability of the L1$_2$ phase.
(2) The increased L1$_2$ phase stability is considered to increase the intermediate-temperature strength of L1$_2$–Co(Al,W) by decreasing the YSA-onset with the increased CSF energy and by increasing the base strength and the extent of yield stress anomaly (at a given temperature) with the increased APB energy on (111).
(3) The increased L1$_2$ phase stability is considered also to increase the high-temperature strength of L1$_2$–Co(Al,W) by increasing the peak temperature with the increased γ'- dissolving temperature so that the peak temperature is not defined by the γ' dissolving temperature unlike in the ternary base compound.
(4) The increased strength of the L1$_2$ strengthening phase due to the increased phase stability thus accounts for the improved creep strength of Co-based superalloys upon alloying with these L1$_2$-stabilizers.

Declaration of Competing Interest

None.

Acknowledgements

This work was supported by Grant-in-Aids for Scientific Research on innovative Areas on High Entropy Alloys through the grant number JP18H-05450 and JP18H-05451, and in part by JSPS KAKENHI grant numbers JP18H01735, JP18H05478, JP19H00824, JP19K22053, JP20K21084, JP21H01651, JP21K14546 and JP22H00262, and by the Elements Strategy Initiative for Structural Materials (ESISM) from the Ministry of Education, Culture, Sports, Science and Technology (MEXT) of Japan (Grant number JPMXP0112101000), and in part by JST-ALCA (Grant Number JPM- JAL1004) and JST CREST (Grant number JPMJCR1994). Dr. N.L. Okamoto of Tohoku University is greatly acknowledged for his help in experiment. HI, MH, UG and GE acknowledge the support from the Alexander von Humboldt Foundation for their cooperative research conducted under the Humboldt Fellowship of HI.

References

[1] J. Sato, T. Omori, K. Oikawa, I. Ohnuma, R. Kainuma, K. Ishida, Cobalt-base high-temperature alloys, Science 312 (2006) 90–91.
[2] A. Bauer, S. Neumeier, F. Pyczak, M. Göken, Microstructure and creep strength of different γ/γ'-strengthened Co-base superalloy variants, Scr. Mater. 63 (2010) 1197–1200.
[3] L. Klein, A. Bauer, S. Neumeier, M. Göken, S. Virtanen, High temperature oxidation of γ/γ'-strengthened Co-base superalloys, Corros. Sci. 53 (2011) 2027–2034.
[4] K. Tanaka, M. Ooshima, N. Tsuno, A. Sato, H. Inui, Creep deformation of single crystals of new Co–Al–W-based alloys with fcc/L1$_2$ two-phase microstructures, Philos. Mag. 92 (2012) 4011–4027.
[5] F. Pyczak, A. Bauer, M. Göken, S. Neumeier, U. Lorenz, M. Oehring, N. Schell, A. Schreyer, A. Stark, F. Symanzik, Plastic deformation mechanisms in a crept L1$_2$ hardened Co-base superalloy, Mater. Sci. Eng. A 571 (2013) 13–18.
[6] C.H. Zenk, S. Neumeier, H.J. Stone, M. Göken, Mechanical properties and lattice misfit of γ/γ' strengthened Co-base superalloys in the Co–W–Al–Ti quaternary system, Intermetallics 55 (2014) 28–39.
[7] F. Xue, H.J. Zhou, Q. Feng, Improved high-temperature microstructural stability and creep property of novel Co-base single-crystal alloys containing Ta and Ti, JOM 66 (2014) 2486–2494.
[8] A. Suzuki, H. Inui, T.M. Pollock, L1$_2$-strengthened Cobalt-base superalloys, Annu. Rev. Mater. Res. 45 (2015) 345–368.
[9] E.A. Lass, D.J. Sauza, D.C. Dunand, D.N. Seidman, Multicomponent γ'-strengthened Co-based superalloys with increased solvus temperatures and reduced mass densities, Acta Mater. 147 (2018) 284–295.
[10] Z. Fan, X. Wang, Y. Yang, H. Chen, Z. Yang, C. Zhang, Plastic deformation behaviors and mechanical properties of advanced single crystalline CoNi-base superalloys, Mater. Sci. Eng. A 748 (2019) 267–274.
[11] Z. Chen, N.L. Okamoto, K. Chikugo, H. Inui, On the possibility of simultaneously achieving sufficient oxidation resistance and creep property at high temperatures exceeding 1000 °C in Co-based superalloys, J. Alloy. Compd. 858 (2020) 157724.
[12] D.W. Chung, J.P. Toinin, E.A. Lass, D.N. Seidman, D.C. Dunand, Effects of Cr on the properties of multicomponent cobalt-based superalloys with ultra high γ' volume fraction, J. Alloy. Compd. 832 (2020) 154790.
[13] H. Zhou, L. Li, S. Antonov, Q. Feng, Sub/micro-structural evolution of a Co–Al–W–Ta–Ti single crystal superalloy during creep at 900 °C and 420 MPa, Mater. Sci. Eng. A 772 (2020) 138791.
[14] F.R. Long, S.I. Baik, D.W. Chung, F. Xue, E.A. Lass, D.N. Seidman, D.C. Dunand, Microstructure and creep performance of a multicomponent Co-based L1$_2$-ordered intermetallic alloy, Acta Mater. 196 (2020) 396–408.
[15] K. Tanaka, T. Ohashi, K. Kishida, H. Inui, Single-crystal elastic constants of Co$_3$(Al,W) with the L1$_2$ structure, Appl. Phys. Lett. 91 (2007) 181709.
[16] M.S. Titus, A. Suzuki, T.M. Pollock, Creep and directional coarsening in single crystals of new γ–γ' cobalt-base alloys, Scr. Mater. 66 (2012) 574–577.

[17] R.C. Reed, The Superalloys, Cambridge University Press, Cambridge, 2006.

[18] A. Bauer, S. Neumeier, F. Pyczak, R.F. Singer, M. Göken, Creep properties of different γ'-strengthened Co-base superalloys, Mater. Sci. Eng. A 550 (2012) 333–341.

[19] Y.M. Eggeler, M.S. Titus, A. Suzuki, T.M. Pollock, Creep deformation-induced antiphase boundaries in $L1_2$ -containing single-crystal cobalt-base superalloys, Acta Mater. 77 (2014) 352–359.

[20] L. Shi, J.J. Yu, C.Y. Cui, X.F. Sun, The creep deformation behavior of a single-crystal Co–Al–W-base superalloy at 900 °C, Mater. Sci. Eng. A 635 (2015) 50–58.

[21] M.S. Titus, Y.M. Eggeler, A. Suzuki, T.M. Pollock, Creep-induced planar defects in $L1_2$-containing Co- and CoNi-base single-crystal superalloys, Acta Mater. 82 (2015) 530–539.

[22] C.H. Zenk, S. Neumeier, N.M. Engl, S.G. Fries, O. Dolotko, M. Weiser, S. Virtanen, M. Göken, Intermediate Co/Ni-base model superalloys-thermophysical properties, creep and oxidation, Scr. Mater. 112 (2016) 83–86.

[23] C.Z. Zhu, R. Zhang, C.Y. Cui, Y.Z. Zhou, F.G. Liang, X. Liu, X.F. Sun, Influence of Ta content on microstructure and creep behavior of a Ni–Co base disc superalloy, Mater. Sci. Eng. A 802 (2021) 140646.

[24] Z.M.T. Chen, N.L. Okamoto, M. Demura, H. Inui, Micropillar compression deformation of single crystals of $Co_3(Al,W)$ with the $L1_2$ structure, Scr. Mater. 121 (2016) 28–31.

[25] N.L. Okamoto, T. Oohashi, H. Adachi, K. Kishida, H. Inui, P. Veyssière, Plastic deformation of polycrystals of $Co_3(Al,W)$ with the $L1_2$ structure, Philos. Mag. 91 (2011) 3667–3684.

[26] H. Mughrabi, The importance of sign and magnitude of γ/γ' lattice misfit in superalloys - with special reference to the new γ'-hardened cobalt-base superalloys, Acta Mater. 81 (2014) 21–29.

[27] M. Ooshima, K. Tanaka, N.L. Okamoto, K. Kishida, H. Inui, Effects of quaternary alloying elements on the γ' solvus temperature of Co–Al–W based alloys with fcc/$L1_2$ two-phase microstructures, J. Alloy. Compd. 508 (2010) 71–78.

[28] S. Kobayashi, Y. Tsukamoto, T. Takasugi, Phase equilibria in the Co-rich Co-Al-W-Ti quaternary system, Intermetallics 19 (2011) 1908–1912.

[29] F. Xue, H.J. Zhou, X.F. Ding, M.L. Wang, Q. Feng, Improved high temperature γ' stability of Co–Al–W-base alloys containing Ti and Ta, Mater. Lett. 112 (2013) 215–218.

[30] H.Y. Yan, V.A. Vorontsov, D. Dye, Alloying effects in polycrystalline γ' strengthened Co–Al–W base alloys, Intermetallics 48 (2014) 44–53.

[31] P.J. Bocchini, C.K. Sudbrack, R.D. Noebe, D.C. Dunand, D.N. Seidman, Effects of titanium substitutions for aluminum and tungsten in Co-10Ni-9Al-9 W (at%) superalloys, Mater. Sci. Eng. A 705 (2017) 122–132.

[32] Z. Fan, C. Wang, C. Zhang, Y. Yu, H. Chen, Z. Yang, The temperature dependence of high-temperature strength and deformation mechanism in a single crystal CoNi-base superalloy, Mater. Sci. Eng. A 735 (2018) 114–120.

[33] A.M.S. Costa, J.P. Oliveira, M.V. Salgado, C.A. Nunes, E.S.N. Lopes, N.V.V. Mogili, A.J. Ramirez, A.P. Tschiptschin, Effect of Ta and Nb additions in arc-melted Co-Ni-based superalloys: microstructural and mechanical properties, Mater. Sci. Eng. A 730 (2018) 66–72.

[34] F. Xue, H.J. Zhou, Q.Y. Shi, X.H. Chen, H. Chang, M.L. Wang, Q. Feng, Creep behavior in a γ' strengthened Co–Al–W–Ta–Ti single-crystal alloy at 1000 °C, Scr. Mater. 97 (2015) 37–40.

[35] M. Yamaguchi, Y. Umakoshi, The deformation behaviour of intermetallic superlattice compounds, Prog. Mater. Sci. 34 (1990) 1–148.

[36] V. Vitek, D.P. Pope, J.L. Bassani, Anomalous yield behaviour of compounds with $L1_2$ structure, in: F.R.N. Nabarro, M.S. Duesbery (Eds.), Dislocations in Solids, Vol. 10. $L1_2$ Oerdered Alloys, Elsevier, Amsterdam, 1996, pp. 135–185.

[37] P. Veyssiere, G. Saada, Microscopy and plasticity of the $L1_2$ γ' phase, in: F.R.N. Nabarro, M.S. Duesbery (Eds.), Dislocations in Solids, Vol. 10. $L1_2$ Ordered Alloys, Elsevier, Amsterdam, 1996, pp. 253–441.

[38] N.L. Okamoto, Y. Hasegawa, W. Hashimoto, H. Inui, Plastic deformation of single crystals of Pt_3Al with the $L1_2$ structure, Philos. Mag. 93 (2013) 60–81.

[39] N.L. Okamoto, Y. Hasegawa, H. Inui, Plastic deformation of single crystals of Pt_3Al with the $L1_2$ structure having a far Al-rich off-stoichiometric composition of Pt-29at.%Al, Philos. Mag. 94 (2014) 1327–1344.

[40] N.L. Okamoto, S. Takemoto, Z.M.T. Chen, M. Yamaguchi, H. Inui, FCC metal-like deformation behaviour of Ir_3Nb with the $L1_2$ structure, Int. J. Plast. 97 (2017) 145–158.

[41] M. Oomae, T. Teramoto, K. Tanaka, Composition dependence of positive temperature dependence of yield stress for $Co_3(Al, W)$–Co_3Ti pseudo-binary alloy with the $L1_2$ structure, Intermetallics 136 (2021) 107250.

[42] S.M. Coplay, B.H. Kear, Temperature and orientation dependence of the flow stress in off-stoichiometric Ni_3Al (γ') phase, Trans. Metall. Soc. AIME 239 (1967) 977–984.

[43] P.H. Thornton, R.G. Davies, T.L. Johnston, The temperature dependence of the flow stress of the γ' phase based upon Ni_3Al, Metall. Trans. 1 (1970) 207–218.

[44] N. Baluc, R. Shäublin, K.J. Hemker, Methods for determining precise values of antiphase boundary energies in Ni_3Al, Philos. Mag. Lett. 64 (1991) 327–344.

[45] D.M. Dimiduk, A.W. Thompson, J.C. Williams, The compositional dependence of antiphase-boundary energies and the mechanism of anomalous flow in Ni_3Al alloys, Philos. Mag. A 67 (1993) 675–698.

[46] Z. Chen, H. Inui, Micropillar compression deformation of single crystals of Fe_3Ge with the $L1_2$ structure, Acta Mater. 208 (2021) 116779.

[47] A. Stroh, Constrictions and jogs in extended dislocations, Proc. Phys. Soc. B 67 (1954) 427.

[48] P.B. Hirsch, A new theory of the anomalous yield stress in $L1_2$ alloys, Philos. Mag. A 65 (1992) 569–612.

[49] V. Paidar, D.P. Pope, V. Vitek, A theory of the anomalous yield behavior in $L1_2$ ordered alloys, Acta Metall. 32 (1984) 435–448.

[50] M.H. Yoo, On the theory of anomalous yield behavior of Ni_3Al - Effect of elastic anisotropy, Scr. Metall. 20 (1986) 915–920.

[51] K.J. Hemker, M.J. Mills, Measurements of antiphase boundary and complex stacking fault energies in binary and B-doped Ni_3Al using TEM, Philos. Mag. A 68 (1993) 305–324.

[52] D. Caillard, J.L. Martin, Thermally Activated Mechanisms in Crystal Plasticity, Pergamon Press, Amsterdam, 2003.

[53] T. Kruml, J.L. Martin, B. Viguier, J. Bonneville, P. Spätig, Deformation microstructures in $Ni_3(Al,Hf)$, Mater. Sci. Eng. A 239-240 (1997) 174–179.

[54] T. Takasugi, O. Izumi, High temperature strength and ductility of polycrystalline Co_3Ti, Acta Metall. 33 (1985) 39–48.

[55] T. Takasugi, S. Hirakawa, O. Izumi, S. Ono, S. Watanabe, Plastic flow of Co_3Ti single crystals, Acta Metall. 35 (1987) 2015–2026.

[56] Y. Liu, T. takasugi, O. Izumi, S. Ono, The peculiar temperature and orientation dependence of $L1_2$-type $Co_{74}Ni_3Ti_{23}$ single crystals, Philos. Mag. A 59 (1989) 401–421.

[57] T. Suzuki, Y. Mishima, S. Miura, Plastic behaviour in $Ni_3(Al,X)$ single crystal - temperature, strain-rate, orientation and composition -, ISIJ Int. 29 (1989) 1–23.